Revealing the dependence of cell spreading kinetics on its spreading morphology using microcontact printed fibronectin patterns

Cheng-Kuang Huang and Athene Donald*
Biological and Soft Systems, Cavendish Laboratory
Department of Physics University of Cambridge

September 23, 2014

Abstract

Since the dawn of the *in vitro* cell cultures, how cells interact and proliferate within a given external environment has always been an important issue in the study of cell biology. It is now well-known that mammalian cells typically exhibit a three phase sigmoid spreading on encountering a substrate. To further these understanding, we examined the influence of cell shape towards the second rapid expansion phase of spreading. Specifically, 3T3 fibroblasts were seeded onto silicon elastomer films made from polydimethylsiloxane, and micro-contact printed with various dimension of fibronectin stripes. Polydimethylsiloxane is adopted in our study for its biocompatibility, its ease in producing very smooth surfaces, and in the fabrication of micro-contact printing stamps. The substrate patterns are compared with respect to their influence on cell spreading over time. Our studies reveal, during the early rapid expansion phase, 3T3 fibroblasts are found to spread radially following a $\simeq t^{1.8}$ law; meanwhile, they proliferated in a lengthwise fashion on the striped patterns, following a $\simeq t^1$ law. We account for the observed differences in kinetics through a simple geometric analysis which predicted similar trends. In particular, a t^2 law for radial spreading cells, and a t^1 law for lengthwise spreading cells.

1 Introduction

In vivo, tissue cells such as fibroblasts, osteoblasts, and other organ tissue cells execute many of their physiological functions whilst in an adherent state. One important function of these tissue cells is in the maintenance of the correct tissue morphology; this must entail intricate application and regulation of force distributions within the tissue, which is only possible if the cells are adherent. To situate themselves correctly, significant cell division, migration, reordering, and differentiation are to be expected before achieving the final configuration. For this active process to result in beneficial outcomes, as in the classic case of embryogenesis where differentiated cells migrate and compartmentalize, there must be considerable coordination between the constituents within the tissue. Indeed, in human wound contractions, where contraction occurs as a consequence of fibroblasts spreading and migrating through the matrix, the outcome is usually less beneficial. This is mainly due to the disordered and over deposition of the connective tissue collagen, and the adverse effects range from minimal cosmetic scars to loss of joint motion or major deformations in the body [1, 2].

*amd3@cam.ac.uk

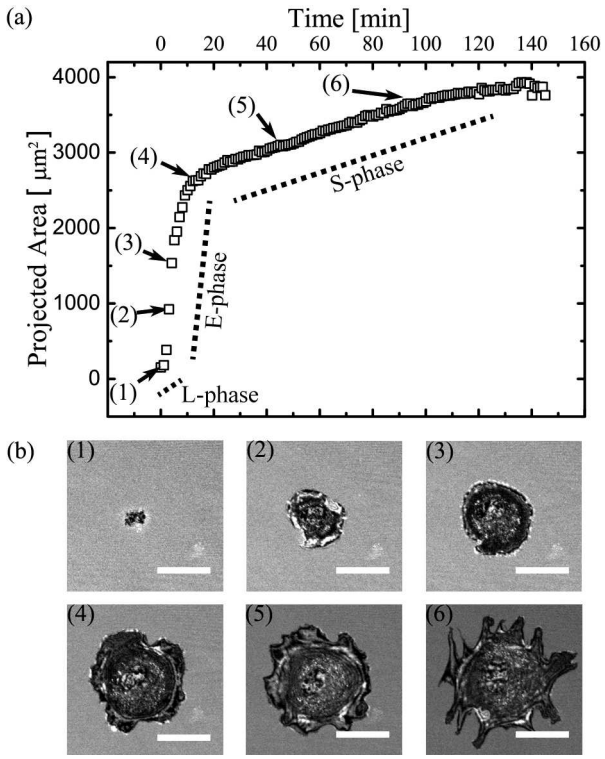

Figure 1: (a) is the RIC derived spread curves of fibroblasts spreading on a PDMS substrate uniformly coated with fibronectin (the control). The dashed lines indicates the phases of the 3T3 spreading: i.e., lag phase (L-phase), rapid expansion phase (E-phase), and steady spreading phase (S-phase). The images in (b) are the associated RIC sequence excerpts labelled in accordance with the numbered points indicated in (a). The scale bars in the RIC images are 30 μm.

Evidently, not limited to the cases just mentioned, the dynamics (and its modulation) of adherent cell spreading and/or locomotion play a critical role in maintaining the normal tissue environment, development, and regeneration; an understanding of which not only is fundamentally interesting, but also has important implications in medical applications.

The substratum supporting such processes in the body typically comprises a 3D matrix of other cells and/or the extracellular matrix (ECM, a fibrous gel like biomaterial composed of collagen, fibrin, fibronectin, and etc.). Thus, to derive dynamical insights into cell spreading and locomotion in these native environments one would ideally wish to be able to obtain 3D images of the cells over time, and with as little a temporal lag between frames as possible. However, there are significant hurdles in accomplishing this in the context of time-lapse live-cell microscopy, as trade-offs between spatial and temporal resolution is an inherent problem in 3D microscopy. It is also foreseeable that the dramatic increase in photon dosage will eventually compromise cell viability over time. Contemplating these present technological limitations, the use of 2D *in vitro* cultures will remain the conventional model in studying the dynamics of adherent cell proliferation. Arguably, the extrapolative value of 2D cell behaviour appears limited at first; nevertheless one can easily envision several situations where a quasi-2D scenario could occur: for example, on the walls of the blood vessels, the epithelium, and on the interfaces of implanted materials.

When adherent cells such as fibroblasts contact 2D surfaces appropriately coated with ECM proteins (cells cannot spread directly on bare external surfaces), they flatten out on the surface over time, through extending higher order filamentous actin (F-actin) structures such as lamellipodia and/or filopodia [3, 4]. The increase of spreading area typically exhibits three major phases: a slow lag phase (L-phase), a rapid expansion phase (E-phase), and a steady-state phase (S-phase) (Fig. 1 (a)). The forces produced through the polymerization of monomeric actins (G-actins) into F-actins—and in turn higher order F-actin constructs—are thought to be the machinery responsible for the spreading and locomotion of adherent cells [5, 6]. Typically, on a smooth substrate that is uniformly and istropically coated with ECM proteins, the membrane enveloping these F-actin structures protrude radially and symmetrically (Fig. 1 (b)) resulting in a uniform expanding disk for the most part of the E-phase. A previous study by Doereiner *et al.* [7] measured a power law exponent in time of $\simeq 1.6 \pm 0.9$ within the E-phase. This result immediately begs the question of whether cells would strive to maintain similar spreading dynamics when spreading anisotropically.

To realize such an anisotropy on a 2D substrate, we incorporated the method of microcontact printing (μCP). It is a useful means of transferring self-assembled monolayers of a variety of molecules, with predefined pattern arrangements, onto surfaces of interest [8]. The process entails the creation of elastomeric stamps (polydimethylsiloxane, PDMS) through standard micro-fabrication techniques, and after inking and drying of relevant molecular species on the stamps, the patterns are transferred by stamping on the substrates. For the purpose of this investigation, ridge-groove structured stamps were created with varying ridge width of 10μm, 25μm, and 50μm. Bovine plasma fibronectin (Sigma-Aldrich, Dorset, UK) were then inked on to the stamps at 50 μg/mL, giving rise to a complete coverage of fibronectin (FN). The patterns are then stamped and transferred on to oxygen plasma-activated thin PDMS films ($\simeq 50\mu$m) fixed in the culturing vessel. The culturing vessel is a stainless steel culture dish with a drilled out base for the purpose of appending spin-coated PDMS films cured on round cover glasses. PDMS, rather than glass or polystyrene, is adopted as the substrate material because of its ease in producing very smooth thin films. Smooth surfaces are desirable in that they help to reduce artefacts arising from cells responding to inherent substrate non-uniformity and textures. The possibility of tuning the stiffness of PDMS also presents potential opportunities in including substrate stiffness as another variable in future studies. In this investigation the stiffest PDMS protocol is used with a Young's modulus akin to that of skin, articular cartilage, and small arteries ($\simeq 10^0$ MPa [9, 10]).

The NIH/3T3 mouse embryonic fibroblasts were seeded onto the PDMS substrates in the culturing vessels and maintained in a live-cell environment on the microscope (confocal scanning laser microscope, Leica TCS SP5) through the use of an enclosing chamber pre-heated to 37 ^{o}C and supplied with 5% CO_2 (Fig. 2). The cell's projected areas were then imaged using reflection interference contrast microscopy (RICM), taking advantage of the superior image contrast in this mode so as to reduce difficulty in the subsequent image segmentation, and thus the extraction of information [11]. Our results from tracking the spreading of these fibroblasts over various fibronectin pattern dimensions do reveal a consistent difference in the dynamics of spreading statistically, and we were able to explain this as due to a geometrically determined power law in time.

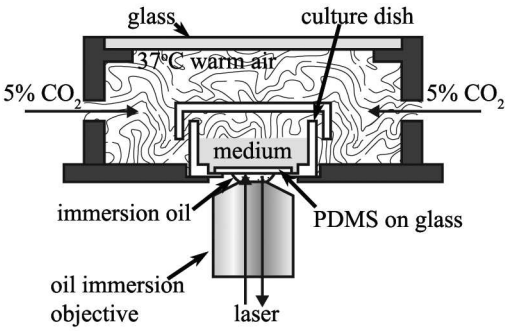

Figure 2: A schematic diagram of the live-cell environment used in maintaining 3T3 viability for extend microscopic observations

2 Results and Discussions

2.1 Morphologically influenced cell spreading kinetics

The graphs in figure 1 (a) and figure 3 (a), (b), and (c) are representative examples of the increase of 3T3's projected area over time (spread curves) for the four substrate conditions; figure 1 (a) shows spreading on the uniformly and isotropically FN coated control surface, and figure 3 (a), (b), and (c) show spreading on the μCP FN stripes. The actual dimension distribution of the stripes, measured from RICM images, are figure 3 (a) 46.7$\pm$1.6 μm (SD), figure 3 (b) 22.9$\pm$1.6 μm (SD), and figure 3 (c) 8.7$\pm$0.9 μm (SD). We shall refer to these as 50, 25, and 10 μm samples for ease of reading. The insets in each graphs are the corresponding RICM live-cell sequence excerpts (Mov. 1-4 in supporting material).

When 3T3 fibroblasts are seeded on to the FN coated PDMS substrates, their initial projected area, as observed through RICM, typically expands in a uniform fashion and in accordance with the underlying pattern: i.e., it expands radially in a circular form on the control substrate (Fig. 1 (b)); and lengthwise in a rectangular form on the striped substrates (insets in Fig. 3 (a), (b), and (c)). It is worth noting that 3T3's on the wider stripes would also spread radially initially, and only expand lengthwise upon reaching the stripe edges. In addition, depending on initial position of the cell relative to an edge, the shape of the initial expanding area may range from fractions of a circle to a full circle (insets in Fig. 3 (a) and (b)). Evident from the later RICM images in the insets, as time progresses, the uniformity and symmetry of the expanding cells' projected area eventually breaks for all the substrate conditions, concurrent with the onset of perimeter undulations of the projected area. The spread curves follow the general three phase sigmoidal trend that has been reported previously [7, 12], with a slow lag (L-phase) leading to a rapid expansion (E-Phase), and tailing off into steady-state spreading (S-Phase). However, in comparing the spread curves for each of the substrate conditions, differences in the gradient of the E-phase is observed. In particular, the E-phase of spreading on the control appear non-linear, whereas similar regions on the spread curve appears linear for spreading on the 10μm stripes. The differences are better revealed on differentiating the spread curves with respect to time. The result are as shown in figure 3 (d). Evidently, cells spreading on the control exhibited a sharp peak within the E-phase, whereas their counterparts spreading on the 10 μm FN stripes exhibited a broader and flatter plateau (dotted line region) within the same phase. Similar characters can also be identified for the spreading on the 50 and 25 μm FN stripes. Additionally, the RICM sequences in the insets

of figure 3 (a) and (b) indicate that the broad plateau is subsequent to the arrival of the spreading front at the stripe boundaries (e.g. point 2 in Fig. 3 (b)).

The general behaviour just described was found to be preserved over the tested sample population in our study; specifically, 24 cells on the control, 25 cells on the 50μm, 23 cells on the 25μm, and 21 cells on the 10μm substrates. An immediate implication of this phenomenon was the possibility that radially spreading cells might reach the S-phase—where F-actin polymerization forces are balanced by the membrane tension—earlier than lengthwise spreading cells. Indeed, if we define the projected area growth duration as the region, on the differentiated curve, between the left peak base and the initial points of an apparent constant 1st derivative (as illustrated in Fig. 4 (a)), the growth durations obtained for radially spreading cells is statistically significantly shorter compared to lengthwise spreading cells (Fig. 4 (b)). Considering the skewed distribution of the data, a non-parametric method, the two-tailed Mann-Whitney U test was employed in assessing the differences. The results revealed $p(=9.0\times10^{-10})<0.0001$ between control and 25 μm stripes; $p(=5.0\times10^{-9})<0.0001$ between control and 10 μm stripes; $p(=0.02)<0.05$ between the 50 μm and 25 μm stripe; and $p(=0.01)<0.05$ between the 50 μm and 10 μm stripe. A significant difference between the control and the 50 μm was also found, $p(=0.0002)<0.001$. This could be explained by the fact that a two behaviour regime can occur on the 50 μm stripes: i.e., smaller cells would behave as if on the control, whilst larger cells would behave as if on the 25 μm stripes. The statistics of the box plots in figure 4 (b) are as summarised in table 1.

2.2 Radial and linear spreading cells obey separate power laws in early E-phase spreading

In order to shed light on the observed phenomenon, a simple analysis of spreading from a geometric perspective was developed. Firstly, in light of the fact that F-actin filaments are ubiquitously involved in cellular locomotion [3, 13] and that pure single F-actin filament elongation also exhibits a similar sigmoid progression over time [14, 15], we formally assumed a prominent, if not exclusive, role of F-actin elongation in cell spreading kinetics. Secondly, it is reasonable to suggest that during the initial spreading, the molecular components responsible for F-actin polymerization such as G-actin, profilin, Arp2/3, and etc. were abundant and isotropically distributed. Thirdly, due to the presence of membrane reservoirs (surface membrane invaginations and/or internal storage of phospholipids) [16, 17], membrane tension should be unimportant at the early stage. Under these circumstance, the F-actin elongation rate should not vary significantly over time within the initial portion of the E-phase of spreading, on all the substrate conditions. Thus, approximating this initial F-actin elongation as constant, one would expect the change in projected area for radially spreading 3T3s on the control substrate to follow

$$\pi r^2 = \pi \times (\alpha_R t)^2 + C, \tag{1}$$

where r is the radius of the projected area, α_R is the radial elongation rate, t is the time, and C is the spreading achieved during the L-phase [18]. By similar analysis, lengthwise spreading 3T3s on the stripes should follow

$$W \times L = 2 \times W \times (\alpha_L t) + C, \tag{2}$$

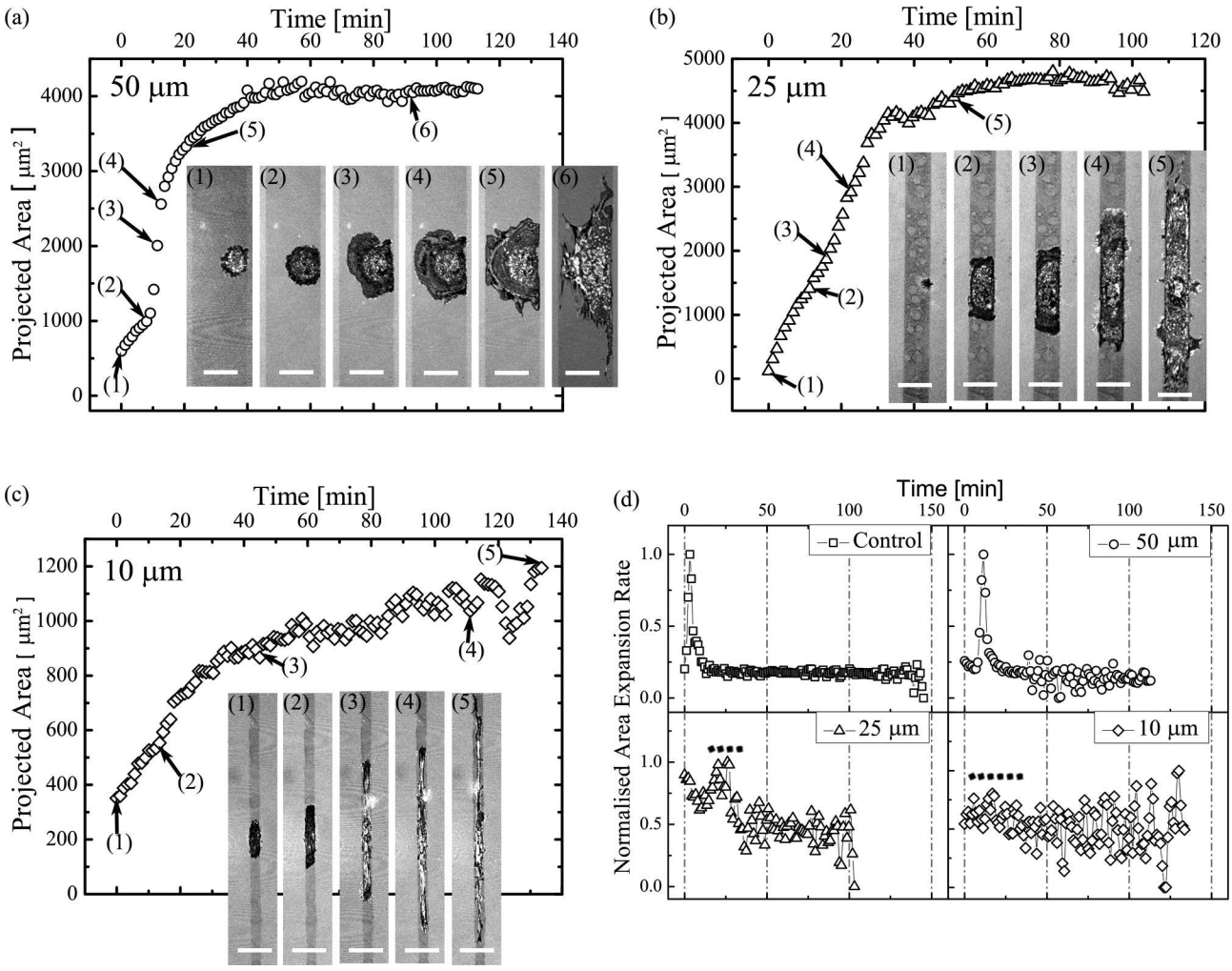

Figure 3: (a), (b), and (c) show the RIC derived spread curves of fibroblasts spreading on the 50, 25, and 10 μm strips of μCP fibronectin, respectively. The insets within each plot are the associated RIC sequence excerpts labelled in accordance with numbered points on the spread curves. The scale bars in the RIC images are all 30 μm. (d) shows the differentiated curves of each of the substrate conditions. The dashed lines indicate regions of apparent linear spreading.

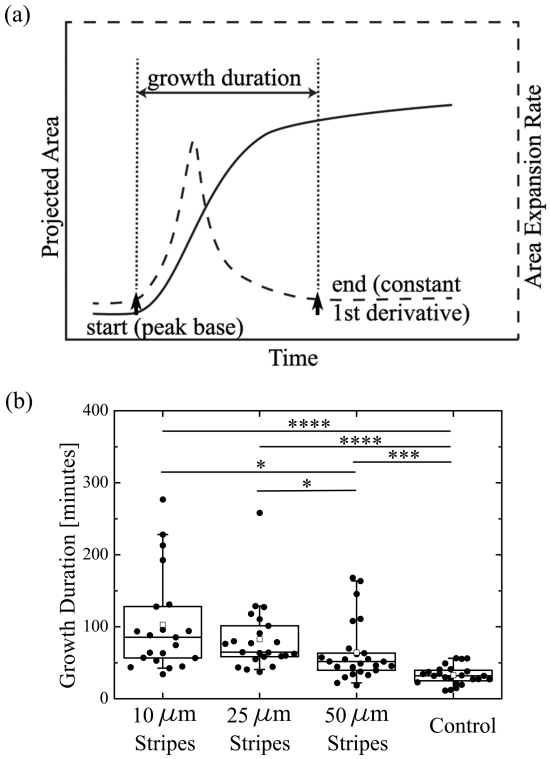

Figure 4: (a) is a schematic illustration of the definition of the growth duration of spreading 3T3s, and (b) shows the statistical distribution of the growth durations over the different substrates (*,p< 0.05; ***,p<0.001; ****,p<0.0001).

Table 1: Statistics of growth durations shown in figure 4 (b)

Substrate	Average Growth Duration min	Median min	Interquartile Range min
Control	32.6±2.6 (SEM)	31.8	14.4
50 μm Stripe	64.3±8.4 (SEM)	51.8	23.9
25 μm Stripe	82.7±9.8 (SEM)	64.6	42.9
10 μm Stripe	102.9±15.0 (SEM)	85.5	71.4

where W is the width of the stripes, L is the long dimension of the projected area, α_L is the longitudinal elongation rate, t is the time, and C here is the spreading attained by the time of reaching the stripe edges. The factor of 2 accounts for the F-actin polymerization occurring at both ends. Clearly, if the assumptions hold, the 3T3's projected area on the control substrate would scale with a power law of t^2. On the other hand, on the stripes, the 3T3 spreading will scale with t. Due to variations typical of biological specimens, we do not presume every cell will follow the predictions strictly, but statistically one would expect the above behaviour. With this in mind, data from the initial portion of the E-phase of the spread curve were compiled for each type of substrate. That is to say, for radially spreading cells, the region between the peak point and its left base point on a differentiated spread curve (Fig. 4 (a), dashed curve), and for lengthwise spreading cells, the region within the width of the broad peak. Regions beyond the peak of the E-phase are excluded, as these regions potentially signify the depletion of the membrane reservoirs and the onset of membrane tension, which ultimately give rise to the S-phase [12, 19].

The results are presented in figure 5 (a), (b), (c), and (d), for the control, the 50 μm, the 25 μm, and the 10 μm substrates respectively. The data have been normalised both in projected area and in time in order to remove intercepts and multiplicative constants. Those E-phases with significantly more data points were uniformly reduced to similar numbers to the majority of other samples to minimise statistical bias in the subsequent non-linear curve fit. An allometric fit of the form $y = x^\beta$ was applied to each dataset, and the exponents, β, obtained were, 1.83±0.06 (SEM) ($R^2 = 0.97$, n=24) for the control (Fig. 5 (a)); 1.82±0.06 (SEM) ($R^2 = 0.94$, n=25) for the 50 μm (Fig. 5 (b)); 0.96±0.01 (SEM) ($R^2 = 0.95$, n=23) for 25 μm (Fig. 5 (c)); and 1.01±0.02 (SEM) ($R^2 = 0.90$, n=21) for 10 μm (Fig. 5 (d)). These results, summarised in table 2, agree well with equations 1 and 2 of our analysis, with only slight deviations. A quantile non-linear regression analysis was also performed on the median of the data, as given in the last column of table 2. The fact that the exponents in the median regression are similar (with the exception of the 50 μm case) to the exponents derived from the general non-linear regression suggests that the skewed distributions found in figure 4 (b) were likely due to a skewed distribution in the coefficient αs or the dynamics in the transitional region between E- and S-phase, rather than in the exponent βs. Again, the exception observed in the 50 μm case is likely due to the two spreading regimes possible depending on the cell size.

The measured 3T3 scaling law on the control substrate also agrees with a previously reported E-phase exponent by Doereiner *et al.* [7], to within their error; in their studies, a power law exponent of $\simeq$1.6±0.9 was obtained. The lower central value can be attributed to the fact that they considered the whole range of the E-phase; this inevitably includes later portions where effects of membrane tension cannot be ignored.

However, $r(t)$ and $L(t)$ in the equations should not be taken to imply that there are well defined multiple single F-actin filaments sprouting from the centres of either case. In fact, as it is often discussed in literature

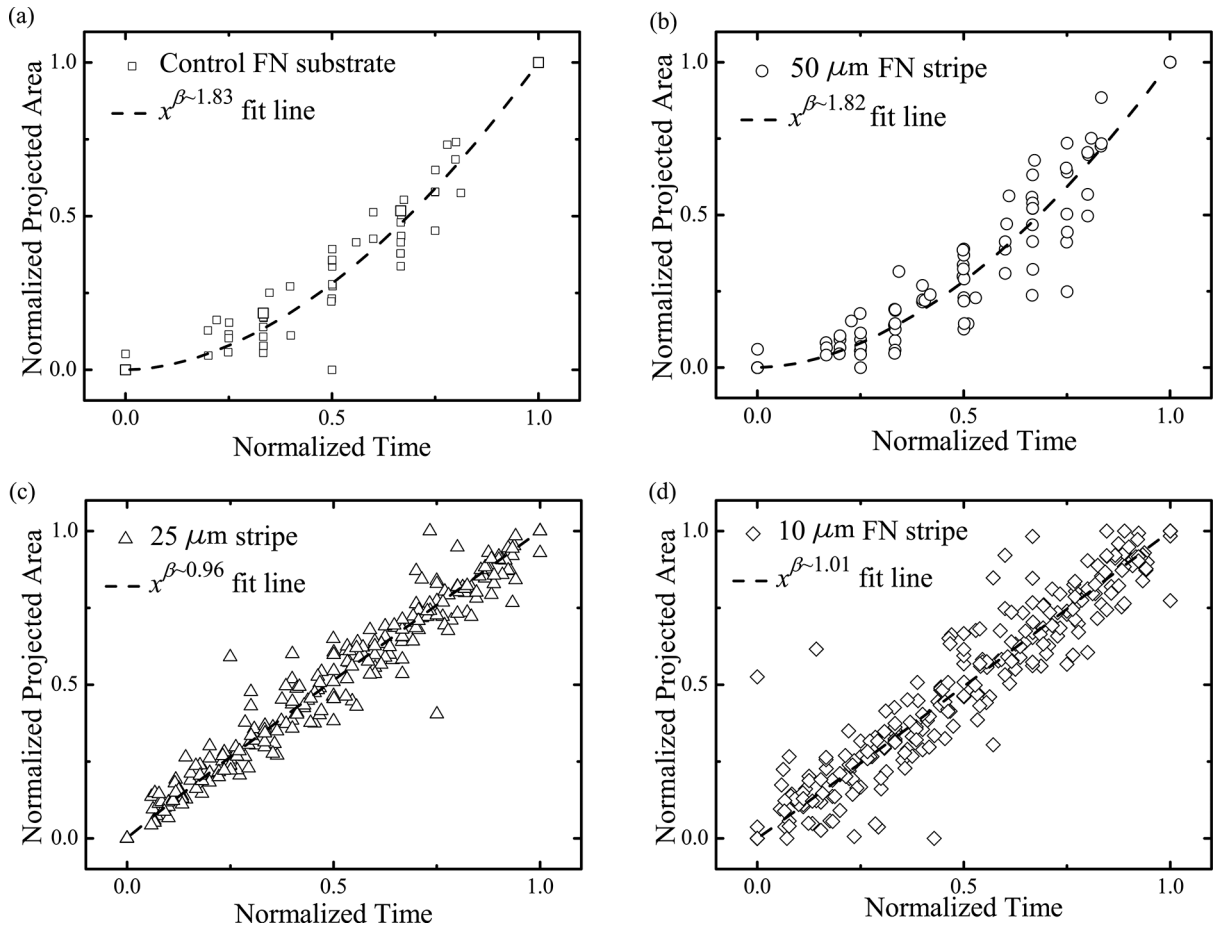

Figure 5: Graphs of concatenated and normalised data extracted from initial portions of the E-phase. (a) control, (b) 50 μm, (c) 25 μm, and (d) 10 μm. The dashed lines are the non-linear fit of $y = x^{\beta}$ on the data.

Table 2: Nonlinear fit using a form of $y = x^{\beta}$

Substrate	Number of Samples	Exponent β	Adjusted R^2	Median Regression β
Control	24	1.83±0.06 (SD)	0.97	1.78±0.11 (SD)
50 μm Stripe	25	1.82±0.06 (SD)	0.94	1.50±0.04 (SD)
25 μm Stripe	23	0.96±0.01 (SD)	0.95	0.97±0.01 (SD)
10 μm Stripe	21	1.01±0.02 (SD)	0.90	1.02±0.02 (SD)

Table 3: F-actin elongation rate derived from Eq. 1 and 2

Substrate	Average F-actin Elongation Rate (subunite/s)	Std. Dev. (subunits/s)
Control	32.3	15.2
50 μm Stripe	25.4	11.8
25 μm Stripe	9.5	5.9
10 μm Stripe	10.1	7.5

[3, 13, 20], lamellipodia, the main contributor to cell spreading and locomotion, is a mesh of short F-actins polymerising from the sides of each other at specific angles. Moreover, this actin structure does not extend all the way back to the centre of the cell. Instead, severing and depolymerisation of the actin branches takes place at the lamellum, about 2 μm in from the leading edge. Further in, the surviving F-actin filaments bundle together to form thick contractile filaments called stress fibres, which also can have a varied directional distribution. The typical arrangement of these higher order F-actin structures are as illustrated in figure 6 (a). Therefore only the rate, the values of αs, are meaningful physically; in that, they predict the barbed end elongation rates of lamellipodia F-actins immediately adjacent to the leading edge.

2.3 Direct observations of the actin kinetics using live-cell fluorescence microscopy and kymographic analysis

To verify this further, we also directly imaged the F-actins in the cell. Specifically, 3T3s were transfected with plasmids encoding the fusion protein and actin marker LifeAct-mTagGFP (p^{CMV}LifeAct-TagGFP2, Thistle Scientific, Glasgow, UK) [21] . The results are as shown in figure 6, where (b) shows a 3T3 fibroblast spreading on a 50 μm FN stripe, and (c) shows one spreading on a control substrate (Mov. 5 and 6 in supporting material). On the left of these images are their corresponding kymographs of the time-lapse sequence, where the height is the time dimension, and the width is the spatial dimension in accordance with the white dashed lines in the main image in (b) and (c). A linear advance of the cell boundaries is immediately apparent in the early spreading, in both cases (white lines). Evidently, an integration of linear elongation over 2π reproduces the results in equation 1.

2.4 Estimating the leading edge barbed-end F-actin elongation rate

Lastly, equations 1 and 2 were used to estimate the leading edge F-actin elongation rates. The rates obtained (using 2.7 nm as the actin subunit length [14]) are as shown in table 3. These rates are higher than previously reported rates of $\simeq$4 subunits/s [15] for purified actin elongation. Considering F-actin elongation is linearly associated with G-actin concentration [22], the discrepancies are reasonable, as cytoplasmic G-actin concentrations are typically on the order of 10^2 μM [23], which is an order or two higher than concentrations used in studying purified actin. However, contrary to our expectation that only the time dependence of increase in area should be modulated by the dimensional restrictions, results in table 3 also showed a clear difference between the F-actin elongation of radially spreading (control and 50 μm) and lengthwise spreading (25 μm and 10 μm) cases ($p<0.0001$ in all comparisons between the radial and the lengthwise spreading): the former is $\simeq$3 $\times$ larger than the latter. With regard to this difference, considering the lowest energy

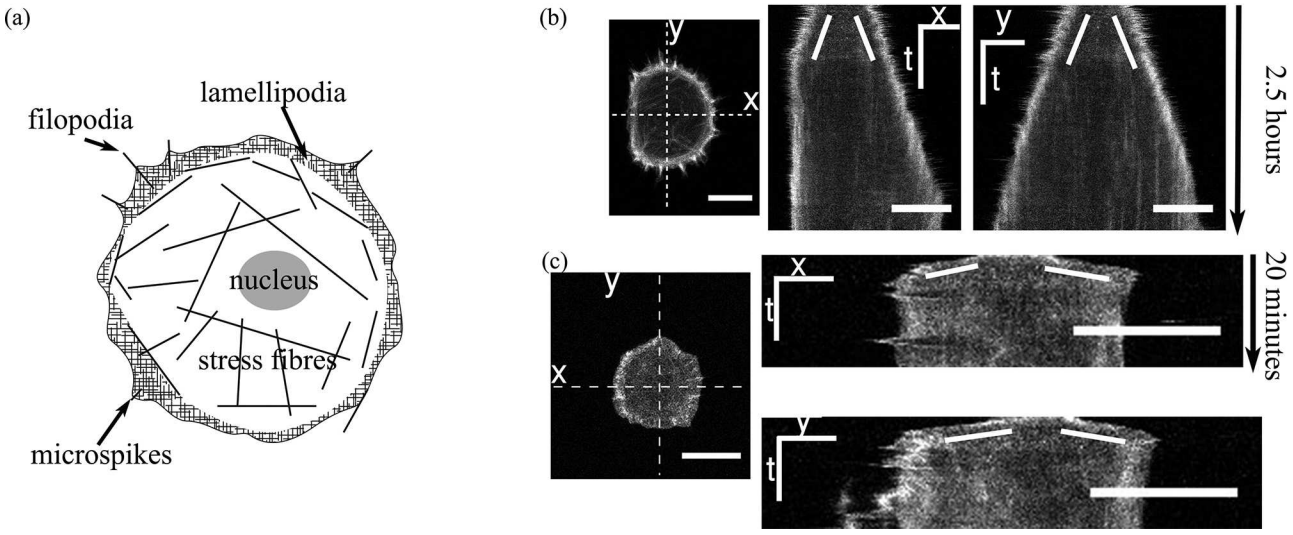

Figure 6: (a) is a schematic illustration of the typical higher order F-actin structures and its distribution; the F-actin structures include lamellipodia, filopodia, and microspikes at the leading edges, and the stress fibres further inwards. (b) and (c) are fluorescent images of 3T3s stably expressing the actin marker, LifeAct-mTagGFP. They are excerpts from the corresponding time-lapse sequence of cell spreading on 50 μm stripes and the control, respectively (see Mov. 5 and 6 in supporting material). Qualitative kinetics of spreading are represented in the kymographs on the left of (b) and (c); the hight represents time and the width represent positions along the white dashed lines in (b) and (c). Kymographs of the horizontal and vertical directions are labelled x and y accordingly. White guide lines indicates the initial linear actin elongation over time. The scale bars in the images are all 30 μm.

configuration of suspended cells is spherical, our speculation is that, when applied to a 2D scenario, a circular disk should correspond to the lower energy configuration. Thus, extra energy costs must be paid in order for the cell to maintain a longitudinal deformation. The effect in turn manifests itself as a reduced initial F-actin elongation rate. The precise mechanisms in which the influence is carried over warrants further investigation.

3 Conclusions

In summary, this investigation has revealed a difference in cell spreading kinetics between radially spreading cells and lengthwise spreading cells. In particular, in the early E-phase, radially spreading cells were found to spread as $\simeq t^{1.8}$, and lengthwise spreading cells spreaded as $\simeq t^1$. The values support our assumptions that spreading in the early E-phase is directly linked to the F-actin elongation rate; it is also consistent with our assumptions that membrane tensions are unimportant in the early stage, and that F-actin associated molecular factors are uniformly distributed. Although the 3T3s were only tested at discrete numbers of pattern dimension, we believe the observed effect is a continuous one, at least for dimensions between the control and the 10 μm pattern: that is, gradually from predominantly radial spreading to predominantly lengthwise spreading. These findings also indicate that adherent cells, fibroblasts at the least, do not self-regulate during early spreading in order to conserve an optimum proliferation rate. Last of all, equations 1 and 2 provide a potential empirical platform for the quantification of the significance of various actin-related molecules previously mentioned; specifically, the elongation constant α can be generalized to a function $\alpha(x_i(t))$ of the concentration of the various influencing factors, $x_i(t)$, at the leading edge.

4 Materials and methods

Cell Culture

NIH/3T3 mouse embryonic fibroblasts (ATCC) were cultured in Dulbecco's modified Eagle's medium (DMEM) (Invitrogen, Paisley, UK) supplemented with 10% fetal bovine serum (Sigma-Alderich, Dorset, UK), and 100 units/mL of penicillin and 100 μg/mL of streptomycin (Sigma-Aldrich, Dorset, UK), at 37 C and 5% CO_2.

Softlithography

Stripe pattern templates, used to create PDMS stamps for micro-contact printing, were fabricated using standard photolithogrphy. The precise steps used is as follows. (1), spin coat photoresist, SU-8 2015 (Chestech Ltd, Rugby, UK), on to a clean silicone wafer (University Wafers, USA) with a 5 second initial spin coat at 500 rpm then ramping up to 2000 rpm for a further 35 seconds; any accumulated photoresists at the edges were carefully scraped off with a razor blade. (2), after a 10 minute re-flow of the SU-8 film, the wafer is pre-baked at 60 ^{o}C for 1 minute, and then at 95 ^{o}C for 2 minutes. (3), when the wafer has cooled, it is placed in a mask aligner (Karl Suss MJB4, Garching, Germany) and brought into soft-contact with the chromium mask (installed prior to placing the wafer) containing the desired stripe array patterns (Compugraphics, Glenrothes, UK). The wafer is subsequently exposed to UV irradiation for 4 seconds. (4), following exposure, the wafer is post-baked at 60 ^{o}C for 1 minute, and then at 95 ^{o}C for 3 minutes to

cross-link exposed SU-8 polymers; again, the wafer is left to cool before the next procedure. (5), to develop the patterns by removing uncross-linked SU-8, the wafer with the SU-8 film is immersed in SU-8 developer (Chestech Ltd, Rugby, UK) and gently agitated for 1 minute. (6), the whole template is rinsed thoroughly with Isopropyl Alcohol, and then blow dried with pressurized nitrogen. (7), the template fabrication is completed by hard-baking the SU-8 template at 150 ^{o}C for 10 minutes to fully cure the SU-8.

The feature height produced using the particular spin coater speed in this protocol is 21.8 $\pm$ 0.9 μm (SD). This is measured from PDMS replicas (described in the following paragraph) of the template by finding the Z positions of reflection planes at different elevations using reflection interference contrast (RIC) microscopy in using a confocal scanning laser microscope (Leica TCS SP5).

To create PDMS stamps for micro-contact printing (μCP), silicone elastomer and curing agent (Sylgard 184, Onecall, Leeds, UK) were first thoroughly mixed in a weight ratio of 10:1 in a glass beaker. Trapped air bubbles are then removed using a vacuum desiccator. On a level surface, the mixture is then poured onto the SU-8 pattern template described previously, to a thickness of around 5 mm; again, any trapped air is removed using vacuum desiccator. Upon reaching a uniform PDMS thickness, the PDMS/template is cured on a hotplate at 150 ^{o}C for 15 minutes. When the PDMS film has cured, it is carefully peeled off the SU-8 template. To complete the process, patterns are cut out into roughly 5 $\times$ 5 mm squares to form the stamps.

Substrate Preparation

The 3T3 cells in this investigation were studied on thin PDMS substrates. To fabricate these substrates, uncured PDMS is first prepared following protocols mentioned previously. It is then poured onto clean 22 mm diameter cover glasses with thickness ranging between 0.16–0.19 mm. The required film thickness is achieved through spin coating the PDMS at 1700 rpm for 35 seconds. The protocol produces PDMS films 55 $\pm$4 (SD, N=14) μm thick. To prevent PDMS flowing back to the centre, it is cured immediately after spin coating, on a hotplate at 150 ^{o}C for 15 minutes.

For time-lapse live-cell imaging of the 3T3 fibroblasts, the prepared PDMS substrates are appended to home-made stainless steel culture dishes with a hole at the bottom designed to accommodate cover glasses; the two parts are bonded together with some more PDMS and cured accordingly.

Micro-contact Printing

Stripe patterns of fibronectin are transferred onto the PDMS substrates through the μCP method. To achieve this, PDMS stamps made earlier were first inked with fibronectin from bovine plasma (Sigma-Alderich, Dorset, UK) at a concentration of 50 μg/mL and incubated for 1 hour at 37 ^{o}C. The stamps is then rinsed three times with 1$\times$ PBS and once with deionized water; this is done by adding drops of the corresponding fluid enough to cover the stamps and waiting a couple of minutes each time. Before applying the stamps to the PDMS substrate, the substrates were first subjected to oxygen plasma treatment (FEMTO Plasma Cleaner, Diener Electronics) for 20 seconds at 100 W and 25 sccm flow rate. This step increases the hydrophilicity of the PDMS surface, and promotes pattern transfer through hydrophilic binding, as it is reasonable to suggest that any hydrophobic binding sites on the fibronectin would already be occupied by the stamp's hydrophobic surface during inking. After plasma treatment, the PDMS stamps are placed into conformal contact with the hydrophilic PDMS substrate. To ensure good pattern transfer, pressure was

briefly applied to the stamps through the use of tweezers. The whole complex is then incubated for three hours at room temperature. Upon removal of the stamps, the PDMS substrate is rinsed with 1× PBS twice. The PDMS substrate is then left overnight for unprinted regions to regain their hydrophobicity; this stalls cell adhesions on unprinted sites and thus bolsters cell confinement.

The actual stripe dimensions produced from the stamp transfer are 46.7±1.6 μm (SD), 22.9±1.6 μm (SD), and 8.7±0.9 μm (SD) for the 50, 25, and 10 μm stamps, respectively. Again, the measurements is performed using RIC microscopy: boundaries of the stripe textures are easily observed due to the reflection interference from monochromatic light reflected off planes either side of the reflection surface.

Transfection of LifeAct-mGFP

In order to visualize F-actin dynamics during a time-lapse live-cell experiment, the 3T3s are transfected with the plasmid p^{CMV}LifeAct-TagGFP2 (Thistle Scientific, Glasgow, UK). The transfection reagent Lipofectamine LTX (Invitrogen, Paisley, UK) was used according to supplier protocol. Briefly, 1 μL of Lipofectamine LTX was diluted in 25 μL Opti-MEM medium (Invitrogen, Paisley, UK). Then, in another vial, 500 ng of plasmid DNA and 0.5 μL of PLUS reagent (Invitrogen, Paisley, UK) was mixed in 25 μL of Opti-MEM medium. Contents of both vials were subsequently combined in a 1:1 ratio. The DNA-lipid complex was incubated for 10 minutes before being added to 3T3s grown to 70–90 % confluency in a 24 well plate containing 500 μL of fresh growth medium. To establish a stable cell line of 3T3s expressing the LifeAct gene, the cells were subjected to selection pressure 48 hours after transfection by adding 1.2 mg/mL of G418 sulfate (Invitrogen, Paisley, UK). Thereafter, the growth medium and antibiotics was replenished every 3 days for 2 weeks. Those cells not expressing the antibiotic resistant gene typically die out within the first week of selection. The stable 3T3s now expressing lifeact-mTagGFP are seeded on to the PDMS substrates and observed dynamically using fluorescence microscopy.

Time-lapse Live-cell Microscopy

Time-lapse live-cell imaging was conducted on a confocal scanning laser microscope (Leica TCS SP5) fitted with an environmental chamber. For a typical experimental session, 3T3 fibroblasts were seeded at a density of 3000 cells/cm^2, with growth medium as described previously, into the stainless steel culture dish containing the μCP PDMS substrate. The sample was immediately placed onto the microscope stage preheated to 37 ^{o}C in the environmental chamber. It is worth noting that growth medium, as opposed to DMEM without serum, is used in the experiments to eliminate any extra effects that might rise from the individual cells responding to serum starvation. From the Vroman effect [24], where plasma proteins with higher mobility do not tend to replace those with lower mobility adsorped on the surface, we presume that serum protein competing with patterned fibronectin would be negligible. This is because the greater part of serum is composed of albumin (e.g. $\simeq$50% in human plasma [25]), which is a much smaller protein ($\simeq$70 kDa) compared to fibronectin ($\simeq$ 440kDa).

Temperature regulation is achieved through the combination of a fan heater and a thermocouple in a feedback circuit that came with the microscope system. A rectangular cover with an optically clear top is then placed over the sample, with 5 % CO_2 feeding into the enclosure through tubes connected to the cover (Fig. 2). The cells were imaged using a 40× oil immersion objective (HCX PL APO CS 40× 1.25NA OIL

UV, Leica), and with a He-Ne 633 nm laser line. The immersion oil used is the type F 1.518 from Leica. The image size was set to 1024×1024 and scanned at a rate of 400 Hz. From these settings and hardware configuration, the size of each pixel translates to 378 nm. Images from reflection interference contrast (RIC) and Differential interference contrast (DIC) were recorded through separate channels by toggling the operating modes in the microscope's LAS AF software suite (Leica). The pinhole size was set to 400 μm to improve the signal-to-noise ratio of RIC images. The time steps in the live-cell recordings are typically set to 1 minute—this preference is a compromise between temporal resolution and the number of locations imaged in a particular live-cell experiment. The 3T3s are typically tracked for 5 hours, as by which point most cells would be well into the steady phase of spreading. A total of 25 3T3s, in five batches of experiment, was tracked on each of the surface conditions.

Fluorescence Microscopy

For the time-lapse live-cell imaging of 3T3 fibroblasts expressing the F-actin binding marker lifeact-mTagGFP, the procedures are for the most part similar to the RIC and DIC imaging previously described. However, an extra channel, in addition to the RIC and DIC channel, is included to visualize the mTagGFP fluorescence. The probe is excited with an 488 nm Argon laser line, and the AOBS filter was shifted to coincide with the emission peak of the probe, which is at 506 nm.

Image Processing

Images exported from the LAS AF software are processed using ImageJ and its various open source plugins. Raw image data are first imported as a time stack and the contrast enhanced using ImageJ's enhance contrast function. Next, positional drifts across the images are re-aligned using the template matching plugin. The image is then segmented using ImageJ's find edge function. Areas enclosed by the cell edges is selected by thresholding the image and using ImageJ's magic wand tool. Selected regions across the stack are saved sequentially, in the region of interest (ROI) manager. Several properties can be derived pertaining to selected regions in the set measurement window; once set, the quantitative data is obtained by using the measure function. With regard to this investigation, the quantities of interest is the 3T3's projected area. Measured data are imported into the data analysis and graphing software OriginPro (OriginLabs), and the projected area is plotted against time; all subsequent statistics and analysis are also done in OriginPro.

5 Acknowledgments

C-K. Huang thank the Ministry of Education in Taiwan, and the Cambridge Overseas Trust for funding his PhD.

References

[1] F. Grinnell, *The Journal of Cell Biology*, 1994, **124**, 401–404.

[2] L. Macintyre and M. Baird, *Burns*, 2006, **32**, 10–15.

[3] J. V. Small, T. Stradal, E. Vignal and K. Rottner, *Trends in Cell Biology*, 2002, **12**, 112–120.

[4] M. Nemethova, S. Auinger and J. V. Small, *The Journal of Cell Biology*, 2008, **180**, 1233–1244.

[5] M. J. Footer, J. W. J. Kerssemakers, J. A. Theriot and M. Dogterom, *Proceedings of the National Academy of Sciences*, 2007, **104**, 2181–2186.

[6] D. A. Fletcher and R. D. Mullins, *Nature*, 2010, **463**, 485–492.

[7] H.-G. Dbereiner, B. Dubin-Thaler, G. Giannone, H. S. Xenias and M. P. Sheetz, *Physical Review Letters*, 2004, **93**, 108105.

[8] M. Mrksich and G. M. Whitesides, *Trends in Biotechnology*, 1995, **13**, 228–235.

[9] I. D. Johnston, D. K. McCluskey, C. K. L. Tan and M. C. Tracey, *Journal of Micromechanics and Microengineering*, 2014, **24**, 035017.

[10] W. M. Saltzman, *Biomedical engineering: bridging medicine and technology*, 2009, p. 366, Cambridge University Press.

[11] A. S. G. Curtis, *The Journal of Cell Biology*, 1964, **20**, 199–215.

[12] M. A. Fardin, O. M. Rossier, P. Rangamani, P. D. Avigan, N. C. Gauthier, W. Vonnegut, A. Mathur, J. Hone, R. Iyengar and M. P. Sheetz, *Soft Matter*, 2010, **6**, 4788–4799.

[13] T. D. Pollard and G. G. Borisy, *Cell*, 2003, **112**, 453–465.

[14] T. D. Pollard, *Analytical Biochemistry*, 1983, **134**, 406–412.

[15] J. R. Kuhn and T. D. Pollard, *Biophysical Journal*, 2005, **88**, 1387–1402.

[16] C. A. Erickson and J. P. Trinkaus, *Experimental Cell Research*, 1976, **99**, 375–384.

[17] D. Raucher and M. P. Sheetz, *Biophysical Journal*, 1999, **77**, 1992–2002.

[18] D. Cuvelier, M. Thry, Y.-S. Chu, S. Dufour, J.-P. Thiry, M. Bornens, P. Nassoy and L. Mahadevan, *Current Biology*, 2007, **17**, 694–699.

[19] D. Raucher and M. P. Sheetz, *The Journal of Cell Biology*, 2000, **148**, 127–136.

[20] S. Nicholson-Dykstra, H. N. Higgs and E. S. Harris, *Current Biology*, 2005, **15**, R346–R357.

[21] J. Riedl, A. H. Crevenna, K. Kessenbrock, J. H. Yu, D. Neukirchen, M. Bista, F. Bradke, D. Jenne, T. A. Holak, Z. Werb, M. Sixt and R. Wedlich-Soldner, *Nature Methods*, 2008, **5**, 605–607.

[22] T. D. Pollard and M. S. Mooseker, *The Journal of Cell Biology*, 1981, **88**, 654–659.

[23] S. A. Koestler, K. Rottner, F. Lai, J. Block, M. Vinzenz and J. V. Small, *PLoS ONE*, 2009, **4**, e4810.

[24] L. Vroman, A. Adams, G. Fischer and P. Munoz, *Blood*, 1980, **55**, 156–159.

[25] A. Farrugia, *Transfusion Medicine Reviews*, 2010, **24**, 53–63.